

WILEY-VCH

 **Chemistry
Europe**

European Chemical
Societies Publishing

Take Advantage and Publish Open Access



By publishing your paper open access, you'll be making it immediately freely available to anyone everywhere in the world.

That's maximum access and visibility worldwide with the same rigor of peer review you would expect from any high-quality journal.

Submit your paper today.



www.chemistry-europe.org



Elucidating the Sectioning Fragmentation Mechanism in Silica-Supported Olefin Polymerization Catalysts with Laboratory-Based X-Ray and Electron Microscopy

Maximilian J. Werny,^[a, b] Dominik Müller,^[c] Coen Hendriksen,^[d] Robert Chan,^[d] Nicolaas H. Friederichs,^[d] Christian Fella,^[e] Florian Meirer,^{*[a]} and Bert M. Weckhuysen^{*[a]}

Strict morphological control over growing polymer particles is an indispensable requirement in many catalytic olefin polymerization processes. In catalysts with mechanically stronger supports, e.g., polymerization-grade silicas, the emergence of extensive cracks via the sectioning fragmentation mechanism requires severe stress build-up in the polymerizing catalyst particle. Here, we report on three factors that influence the degree of sectioning in silica-supported olefin polymerization catalysts. Laboratory-based X-ray nano-computed tomography (nanoCT) and focused ion beam-scanning electron microscopy (FIB-SEM) were employed to study catalyst particle morphology and crack propagation in two showcase catalyst systems, i.e., a

zirconocene-based catalyst (i.e., Zr/MAO/SiO₂, with Zr = 2,2'-biphenylene-bis-2-indenyl zirconium dichloride and MAO = methylaluminoxane) and a Ziegler-Natta catalyst (i.e., TiCl₄/MgCl₂/SiO₂), during slurry-phase ethylene polymerization. The absence of extensive macropores in some of the catalysts' larger constituent silica granulates, a sufficient accessibility of the catalyst particle interior at reaction onset, and a high initial polymerization rate were found to favor the occurrence of the sectioning pathway at different length scales. While sectioning is beneficial for reducing diffusion limitations, its appearance in mechanically stronger catalyst supports can indicate a suboptimal support structure or unfavourable reaction conditions.

Introduction

Industrial olefin polymerization catalysts are well-established catalyst materials that have been in use for decades to produce some of mankind's most in demand high-performance materials, such as polyethylene and polypropylene.^[1] Despite the associated research field being quite mature, further insights into the functionality of these 'single-use' systems at the onset of polymerization remain highly desirable. It is during this critical stage that both the activity and final product morphology are determined by the concurrently occurring processes of polymer formation and support fragmentation.^[2] The stress-induced 'breaking apart' of the catalyst support not only exposes new active sites, but is also instrumental in overcoming mass and heat transfer limitations.^[3,4] Thus, to rationally design the next generation of supported olefin polymerization catalysts, it is paramount to further characterize and elucidate support fragmentation from a mechanistic point of view.

Various accounts from literature,^[2,4-8] including recent studies by our group,^[9-13] report on the synergy of the layer-by-layer and sectioning mechanisms in facilitating the morphological evolution of supported olefin polymerization catalysts. Depending on the type of support and the reaction conditions that are employed, the contributions of either mechanism may become dominant (Figure 1). For instance, various groups have reported an instantaneous break-up of the relatively fragile MgCl₂ support in conventional Ziegler-Natta catalysts during propylene polymerization (Figure 1, particle morphologies **a** and **b**).^[8,14-18] Recent high-resolution 3D tomography studies on the fragmentation of comparable MgCl₂-supported Ziegler-Natta and Ziegler-type catalysts, employed in slurry-phase propylene and ethylene polymer-


[a] M. J. Werny, Dr. F. Meirer, Prof. B. M. Weckhuysen
Inorganic Chemistry and Catalysis
Debye Institute for Nanomaterials Science
Utrecht University
Universiteitsweg 99
3584 CG Utrecht (The Netherlands)
E-mail: b.m.weckhuysen@uu.nl
f.meirer@uu.nl


[b] M. J. Werny
Dutch Polymer Institute (DPI)
P.O. Box 902
5600 AX Eindhoven (The Netherlands)


[c] D. Müller
Lehrstuhl für Röntgenmikroskopie
Universität Würzburg
Josef-Martin-Weg 63
97074 Würzburg (Germany)

[d] Dr. C. Hendriksen, R. Chan, N. H. Friederichs
SABIC Technology Center
Urmonderbaan 22
6167 RD Geleen (The Netherlands)

[e] Dr. C. Fella
Fraunhofer IIS
Josef-Martin-Weg 63
97074 Würzburg (Germany)

 Supporting information for this article is available on the WWW under <https://doi.org/10.1002/cctc.202200067>

 This publication is part of a joint Special Collection with EurJOC and EurJIC on the Netherlands Institute for Catalysis Research. Please see our homepage for more articles in the collection.

 © 2022 The Authors. ChemCatChem published by Wiley-VCH GmbH. This is an open access article under the terms of the Creative Commons Attribution License, which permits use, distribution and reproduction in any medium, provided the original work is properly cited.

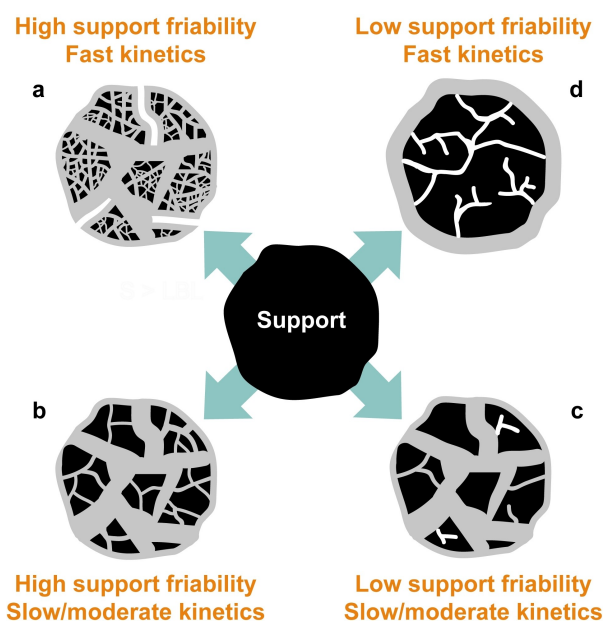


Figure 1. Schematic of the sectioning mechanism's contributions during catalytic olefin polymerization (black, support; gray, polymer; white, formed cracks; pores are not shown for simplification). The relative involvement of the sectioning mechanism is influenced by the friability of a catalyst's support, the catalyst's kinetics and the applied reaction conditions. Significant mass transfer limitations and stress generation lead to pronounced manifestations of the sectioning mechanism (particle morphologies a and d), while less pronounced mass transfer limitations and stress generation will lead to a more controlled fragmentation of the support, often involving the layer-by-layer mechanism (not shown for simplification) to a comparatively large extent (particle morphologies b and c). The morphologies displayed above represent simplified showcases (post reaction onset) and do not address the full complexity of experimentally observed support fragmentation.

ization, further confirmed that the sectioning mechanism is heavily involved in MgCl_2 -supported systems.^[9,10] In contrast to this, the fragmentation of metallocene-based catalysts, usually supported on mechanically firmer, less fragmentable SiO_2 supports, is often dominated by the layer-by-layer mechanism at the particle surface as well as at the level of the support's constituent granulates or domains, especially during ethylene polymerization (Figure 1, particle morphology c).^[6,11,12,19,20] Irrespective of the type of support, industrial operating conditions (i.e., high pressures and temperatures) or highly active catalytic sites can lead to more extensive contributions from the sectioning mechanism as a result of pronounced polymer build-up, mass transfer limitations and stress accumulation (e.g., particle morphologies a and d in Figure 1).^[8,11,12]

To obtain novel insights into the origins of the sectioning fragmentation mechanism, we investigated two industrial-gradesilica-supported olefin polymerization catalysts, namely a zirconocene-based catalyst (i.e., $\text{Zr}/\text{MAO}/\text{SiO}_2$, with $\text{Zr} = 2,2'$ -biphenylene-bis-2-indenyl zirconium dichloride and $\text{MAO} = \text{methylaluminumoxane}$) and a Ziegler-Natta catalyst (i.e., $\text{TiCl}_4/\text{MgCl}_2/\text{SiO}_2$), that were both used in slurry-phase ethylene polymerization. The catalysts' respective morphologies were assessed using a combination of laboratory-based nano-computed tomography (nanoCT) and focused ion beam-scanning electron microscopy (FIB-SEM)

(Figure S1). While FIB-SEM is widely employed for the morphological analysis of heterogeneous catalysts,^[21–26] high resolution laboratory-based nanoCT represents a less frequently used yet accessible methodology for obtaining structural information and chemical information in 3D. In recent years, nanoCT has successfully been employed to characterize a supported liquid metal catalyst for alkane dehydrogenation,^[27] a zeolite material,^[28] as well as electrochemical devices such as fuel cells.^[29,30]

From an instrumental point of view, a handful of different technologies exist for laboratory-based nanoCT. This includes lens-based full-field microscopes^[28,31] as well as devices that operate in projection-based magnification, either featuring adapted SEM devices as the source^[32] or a nanofocus X-ray source.^[33] These devices can achieve 3D resolutions in the range of 50–150 nm. Due to the availability of various imaging technologies with different photon energies and fields of view, the choice of instrument ultimately depends on the sample and the required imaging parameters.

The CT set-up employed in this study features a nanofocus X-ray source, covering an energy range of 5–110 keV.^[33–35] A variety of samples can be imaged under ambient conditions at 2D and 3D spatial resolutions of up to 150 nm and 170 nm, respectively.^[33–35] Specifically in the context of supported olefin polymerization catalysts, the technique delivers comprehensive information on the extent and magnitude of large-scale fragmentation phenomena (i.e., crack formation and propagation) and the 3D structure and phase distribution of individual particles^[24,36,37] – more so than other laboratory-based techniques such as SEM, which only yields 2D information.^[11,17,19,38–42]

Thus, by using nanoCT in combination with FIB-SEM, we were able to identify three important factors that, in addition to the friability of a given support, are responsible for suboptimal monomer diffusion and stress generation, thus leading to a more frequent occurrence of the sectioning fragmentation mechanism in silica-supported olefin polymerization catalysts. The three contributing factors that we will discuss in this work are: (i) A low degree of macroporosity at the level of the constituent support domains or particle level, (ii) a high particle accessibility during the initial reaction stages, and (iii) fast catalyst kinetics.

Results and Discussion

The two silica-supported olefin polymerization catalysts under study ($\text{Zr}/\text{MAO}/\text{SiO}_2$, $\text{TiCl}_4/\text{MgCl}_2/\text{SiO}_2$) were synthesized according to two different procedures (Section S1 of the Supporting information, SI). Despite both catalysts being composed of compositionally identical polymerization-grade silicas with the same pore volume and surface area (refer to Figures S2 and S3 for external and internal particle morphologies), the average particle sizes of the silica supports ($\text{Zr}/\text{MAO}/\text{SiO}_2$: $D_{50} = 25 \mu\text{m}$, $\text{TiCl}_4/\text{MgCl}_2/\text{SiO}_2$: $D_{50} = 50 \mu\text{m}$) and, moreover, the chemical compositions of the supported metal-organic phases, differ significantly. It is thus difficult to draw parallels between these two catalyst systems when determining structure-activity correlations. However, novel insights related to the sectioning fragmentation mechanism were gained from investigating the morphologies of both catalysts.

These are presented side-by-side to deliver a comprehensive overview of the different factors that can contribute to the sectioning pathway.

The catalysts were primarily studied after slurry-phase ethylene polymerization at room temperature and different pressures. Pre-polymerizations were performed for short time periods in an autoclave reactor at 7.5–15 bar ethylene, or in a fume hood-based polymerization set-up at ambient pressure, with the latter used to obtain low polymer yield samples ($\leq 6.4 \text{ g}_{\text{PE}}/\text{g}_{\text{cat}}$, PE = polyethylene; Table 1, SI Section S2).

Absence of large macropores promotes sectioning in the catalyst support granulates

The silica-supported zirconocene-based catalyst was pre-polymerized for 1 min in slurry-phase at 10 bar and 15 bar ethylene pressure in the presence of low amounts of tri-isobutylaluminum (TiBA) as scavenger (obtained yield for both reactions: $2.1 \text{ g}_{\text{PE}}/\text{g}_{\text{cat}}$, SI Section S2). NanoCT was employed to characterize the 3D morphology of four particles from the sample pre-polymerized at 10 bar (Zr_{10-1} – Zr_{10-4}) at sub-180 nm spatial resolution (Figure S4). The tomographies and reconstructed cross-sections (i.e., virtual slices) of particles Zr_{10-1} – Zr_{10-4} (Figures 2a and S5, Supplementary Videos S1 and S2) show that the catalyst particles' respective surfaces as well as large portions of their interiors have fragmented due to the formation of polymer, presumably following the layer-by-layer mechanism.^[11,12]

The reconstructions of particles Zr_{10-1} and Zr_{10-2} , however, also clearly indicate a parallel involvement of the sectioning mechanism at silica granulate level, as is schematically illustrated in Figure 1 (particle morphology c). Several larger silica domains, visibly lacking large macropores, have been penetrated and divided by extensive cracks (indicated by white arrows in Figure 2a, Supplementary Video S1). Sectioning in these polymer-embedded support granulates is attributed to the build-up of relatively large amounts of strain within the polymerizing particle. The support domains lack extensive macropore networks (Supplementary Video S1), which resulted in a lower accessibility of their active sites and increased the probability of significant local mass transfer limitations. The sectioning of the silica granulates effectively helped in overcoming these mass transfer limitations while instantaneously exposing a large amount of 'buried' active sites, which subsequently participate in the polymerization reaction. Contributions from the sectioning mechanism at the

scale of several microns are vital for overcoming mass transfer limitations, especially under vigorous reaction conditions, i.e., at high monomer concentrations and temperatures, or in the presence of highly active catalytic sites.

To verify our assumptions, FIB-SEM was performed on the two pre-polymerized catalyst batches (i.e., 10 and 15 bar; Figure 2b). All catalyst particles, to different extents, featured contributions from the sectioning mechanism. While its involvement may be subtle in the case of particle Zr_{10-5} , it is much more apparent in the remaining particles (Zr_{10-6} , Zr_{15-1} and Zr_{15-2}). Significant cracks were presumably formed in the affected domains due to high polymerization activity in adjacent regions (Zr_{10-5} , Zr_{10-6}), inherent structural weaknesses of the support (e.g., in close vicinity to the macropore space; Zr_{15-1}) as well as high polymerization rates at the particle surface (Zr_{15-1} , Zr_{15-2}). With most of the affected support domains lacking significant macroporosity, mass transport is limited, hence leading to more pronounced stress generation and crack formation. The effect of severe mass transfer limitations is particularly obvious in particle Zr_{15-2} , which is cleaved by a substantial crack. This may have been related to a rapid build-up of polymer at the particle surface at high ethylene pressure (15 bar). With certain domains of the particle continuing to react, albeit at presumably lower rates, significant stress may have generated. This leads to a severe rupturing of the silica domain. Significant localized stress build-up and concurrent sectioning are also apparent in particles pre-polymerized at 1.6 bar ($2.1 \text{ g}_{\text{PE}}/\text{g}_{\text{cat}}$, Table S1; Figure S6), suggesting that the sectioning mechanism does also contribute to a certain extent under milder conditions (i.e., at lower ethylene pressure and thus concentration). In general, this form of sectioning can take place at any stage of the reaction, provided mass transfer limitations and stress build-up are sufficient. Naturally, mass transfer limitations will be larger at higher polymer yields.

High initial catalyst particle accessibility facilitates surface-based sectioning

To study the morphology of the Zr/MAO/SiO₂ catalyst at reaction onset, it was pre-polymerized in slurry-phase for 45 s at 1 bar ethylene pressure (SI Section S2). Interestingly, a pronounced fragmentation of some of the particles' surfaces was observed (Figure 3). Due to the dimensions and spatial arrangement of the cracks, the process can be defined as surface-based sectioning. Strands of polyethylene are visible in these cracks (Figure 3, close-ups of particles Zr_{1-1} and Zr_{1-2} , outlined in orange) and were presumably formed due to polymerization in the sub-surface layers of the particle. Subsequent crack formation caused the PE to be stretched.^[43] Polymer fibrils are also visible at the surface of particle Zr_{1-1} , (see areas in close vicinity to crack in close-up image), which rules out the scenario of extensive surface deactivation.^[11]

Comparable particle morphologies, in terms of crack formation, have been reported by the group of McKenna, who used short stop reactors to pre-polymerize silica- and MgCl₂-supported olefin polymerization catalysts for extremely short reaction periods at elevated pressures.^[8,44–46] Similar observations were also made by Weist *et al.* for a silica-supported Phillips-type catalyst pre-

Table 1. Overview of the conditions employed during the slurry-phase pre-polymerizations reactions as well as the corresponding catalyst yields.

Catalyst	p(C ₂ H ₄) [bar]	t [min]	T [°C]	n(TiBA):n [M]	Yield [g _{PE} /g _{cat}]
Zr/MAO/SiO ₂	10	1	25	0.36	2.1
	15	1	25	0.36	2.1
	1	0.75	25	0	1.1 ^[a]
TiCl ₄ /MgCl ₂ /SiO ₂	7.5	1	25	6.50	6.4

[a] PE yield determined from the D₅₀ of the pre-polymerized catalyst sample, see SI Section S2.

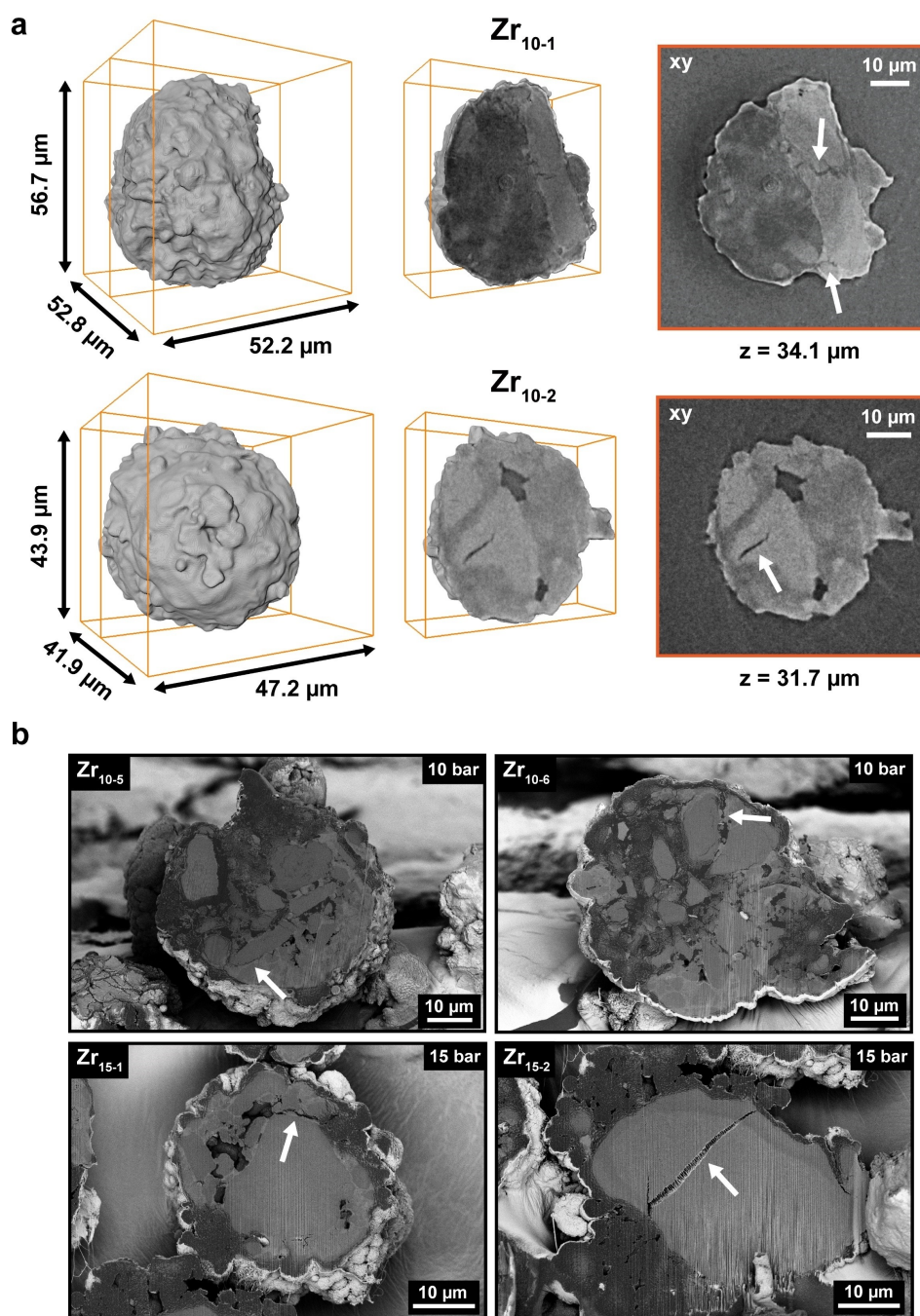


Figure 2. Morphological characterization of the Zr/MAO/SiO₂ catalyst (MAO = methylaluminoxane) after slurry-phase pre-polymerization for 1 min at 10 bar and 15 bar ethylene pressure, respectively (room temperature, obtained yields: 2.1 g_{PE}/g_{cat}): (a) Reconstructed tomographies and corresponding virtual cross-sections of the two particles Zr₁₀₋₁ and Zr₁₀₋₂ from the 10 bar pre-polymerized batch. The light gray phase can be classified as support-dominant phase, while the dark gray phases correspond to the remaining particle volume (i.e., polymer-dominant phase + pore space). *z* is the depth of a given cross-section (*xy*) with *z* = 0 μm corresponding to the top of the particle. The formation of large cracks (i.e., sectioning) is indicated by white arrows. (b) Scanning electron microscopy (SEM; light gray, silica support; dark gray, polymer) images of selected catalyst particle cross-sections from the 10 bar (Zr₁₀₋₅, Zr₁₀₋₆) and 15 bar (Zr₁₅₋₁, Zr₁₅₋₂) batches.

polymerized in gas-phase at 1 bar ethylene pressure.^[47] The formation of these cracks is presumed to be caused by the diffusion of ethylene throughout the macroporous catalyst particle, consequently leading to polymerization activity at all accessible active sites within the particle. The resulting strain from the expanding polymer-silica composite matrix initiates the large-

scale fragmentation of the catalyst particles by opening up the compact catalyst support, exposing previously buried active sites and further enhancing the accessibility of the particle's interior for the incoming monomer. This is, in fact, evident from the cross-sectional analysis of a catalyst particle displaying surface fractures (Zr₁₋₃). The formation of polymer in the particle interior has led to

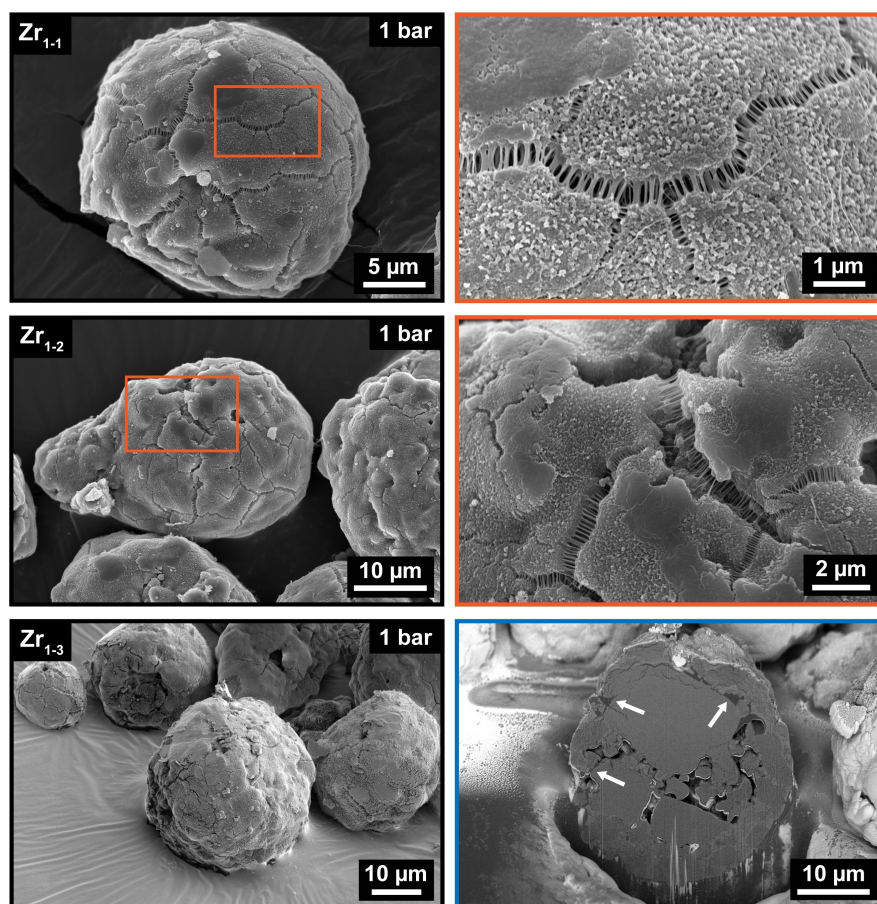


Figure 3. Morphological characterization of the Zr/MAO/SiO₂ catalyst (MAO = methylaluminoxane) that was pre-polymerized in slurry-phase at 1 bar ethylene pressure (45 s, room temperature, estimated yield: 1.1 g_{PE}/g_{cat}): Scanning electron microscopy (SEM; light gray, silica support; dark gray, polymer) images of catalyst particles Zr₁₋₁, Zr₁₋₂ and Zr₁₋₃, including zoom-ins of catalyst particles Zr₁₋₁ and Zr₁₋₂ (orange) as well as the cross-section of catalyst particle Zr₁₋₃ (blue). In the latter, formed polymer is indicated by white arrows.

significant stress-build up and fragmentation in the outer sphere of the catalyst particle (Figure 3, indicated by white arrows in the corresponding SEM image, outlined in blue; also refer to Figure S7). We believe that this form of fragmentation generally requires a high accessibility of the catalyst particle interior at the beginning of the reaction to ensure sufficient polymer formation in the interior. At higher ethylene pressures or at more advanced reaction stages, the accumulation of polymer at the particle surface is likely to fill the cracks. Fast catalyst kinetics may even reduce the accessibility of the particle interior at reaction onset to such an extent that surface-based sectioning is suppressed.

Fast polymerization kinetics induce sectioning at the catalyst particle level

The sectioning mechanism was observed to play an instrumental role in the morphological evolution of a silica-supported Ziegler-Natta catalyst (TiCl₄/MgCl₂/SiO₂), pre-polymerized in slurry-phase for 1 min at 7.5 bar ethylene pressure (obtained yield: 6.4 g_{PE}/g_{cat}, Table 1). Before introducing ethylene, the catalyst was pre-contacted with 6.5 eq. TiBA (co-catalyst) in heptane for approx-

imately 10 min (SI Section S2). The catalyst's productivity (i.e., polyethylene yield) implies that the catalyst is kinetically faster than the Zr/MAO/SiO₂ catalyst (TiCl₄/MgCl₂/SiO₂, 6.4 g_{PE}/g_{cat}, 7.5 bar, 1 min; Zr/MAO/SiO₂, 2.1 g_{PE}/g_{cat}, 10 bar, 1 min; Tables 1 and S1). This was corroborated with diffuse reflectance infrared Fourier transform spectroscopy (DRIFTS), which delivered kinetic data on the formation of PE on the catalyst bed surface during gas-phase ethylene polymerization (Figure 4, refer to Experimental Section for more details). As can be seen in Figures 4a and 4b, the introduction of gaseous ethylene (see vibrational and roto-vibrational modes between 2980 and 3200 cm⁻¹) leads to the emergence of several bands in the ν(CH₂) spectral region (2800–3000 cm⁻¹),^[48,49] indicative of methylene (CH₂) and methyl (CH₃) groups and thus the growth of PE chains. The rate of PE formation was calculated by integrating the ν_s(CH₂) band at 2851 cm⁻¹ in the background corrected and fitted spectra (Figures 4a, 4b, S8 and S9) and subsequently forming the first time derivative thereof. As is evident in Figure 4c, the activity of the Ziegler-Natta catalyst increases significantly within the first 1.5 min of polymerization, especially when compared to the, under these conditions, markedly slower Zr/MAO/SiO₂ catalyst (Figure 4b). In fact, the technique can only be used to monitor the start of the polymer-

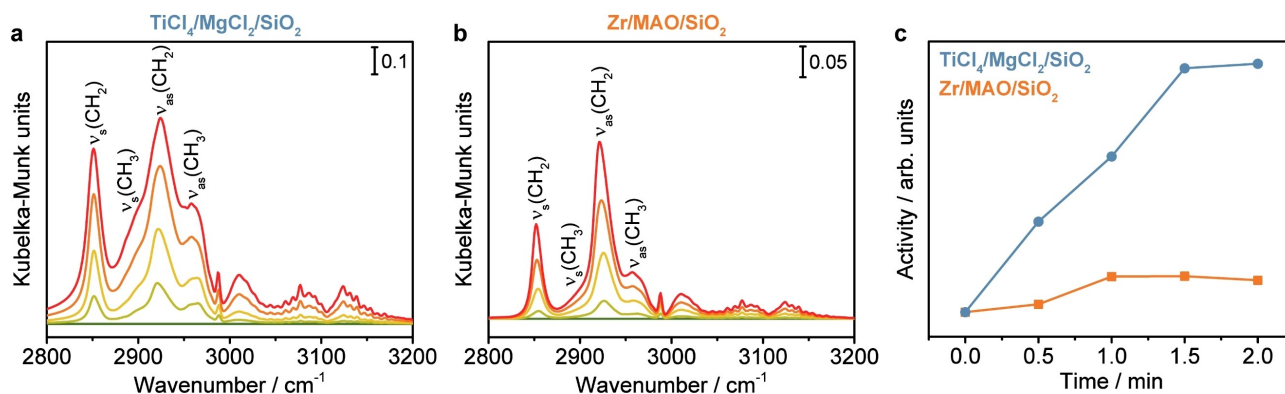


Figure 4. Diffuse reflectance infrared Fourier transform spectroscopy (DRIFTS) data collected on the $\text{TiCl}_4/\text{MgCl}_2/\text{SiO}_2$ (1.5 eq. triisobutylaluminum, TiBA) and $\text{Zr}/\text{MAO}/\text{SiO}_2$ catalysts (MAO = methylaluminoxane) during gas-phase ethylene polymerization (1 bar ethylene, 5 mL/min, room temperature, 12 mg catalyst): (a) Background subtracted DRIFTS spectra of the $\text{TiCl}_4/\text{MgCl}_2/\text{SiO}_2$ catalyst (5 spectra, 2.0 min reaction time, transition from green to red), (b) Background subtracted DRIFTS spectra of the $\text{Zr}/\text{MAO}/\text{SiO}_2$ catalyst (5 spectra, 2.0 min reaction time, transition from green to red), and (c) Activities of the two catalysts plotted versus time, based on individual testing runs. The activities of the catalysts were determined as the time derivative of the $\nu_s(\text{CH}_2)$ stretching vibration band (2851 cm^{-1}) area, which represents the rate of polyethylene formation on the catalyst bed surface (refer to Experimental Section). Only spectra recorded in the first 2.0 min of ethylene polymerization were used for comparison due to an oversaturation of the IR signal after 2.0 min in the case of the $\text{TiCl}_4/\text{MgCl}_2/\text{SiO}_2$ catalyst (high rate of PE formation).

ization reaction on the $\text{TiCl}_4/\text{MgCl}_2/\text{SiO}_2$ catalyst as the catalyst bed rises within minutes due to PE formation (Figure S10), leading to a strong baseline drift in the recorded spectra and an oversaturation of the IR signal. The relative decrease in activity after 1.5–2 min may be attributed to the onset of mass transfer limitations that are typical for this reaction stage (i.e., the pre-polymerization and induction regimes).^[19]

To assess the impact of the $\text{TiCl}_4/\text{MgCl}_2/\text{SiO}_2$ catalyst's markedly faster rate of PE formation, the morphologies of two pre-polymerized catalyst particles were assessed with nanoCT ($\text{ZN}_{7.5-1}$, $\text{ZN}_{7.5-2}$; Figure 5a, Supplementary Video S3). Both particles feature distinct shells of polyethylene that were formed via polymerization and layer-by-layer fragmentation in the peripheral regions of the particles. SEM images taken at an earlier reaction stage indicate that the polyethylene shell is directly formed upon exposure to ethylene (Figure S11). Since the polymer shell is formed at reaction onset, the access of both the monomer (i.e., ethylene) and the co-catalyst (i.e., TiBA) to the particle interior is restricted at an early reaction stage.^[50]

In addition to the surface build-up of polyethylene, the particles possess radial fractures ($> 10\ \mu\text{m}$ in size) that are indicative of the sectioning fragmentation mechanism (indicated by white arrows in Figure 5a, Supplementary Video S3). Most notably in $\text{ZN}_{7.5-2}$, substantial crack formation is observed throughout the silica support. The cracks propagate several microns through the particle, thus suggesting that significant strain was generated due to polymer build-up and concurrent polymerization activity in the particle interior.

Similar morphologies were also observed for other catalyst particles with FIB-SEM. As can be seen in Figure 5b, the remaining silica supports (light gray) of particles $\text{ZN}_{7.5-3}$ and $\text{ZN}_{7.5-4}$ feature extensive cracks and are enveloped by thick layers of polyethylene (dark gray), leading to higher stress accumulation and lower stress dissipation within the particle (Figure 1, particle morphology d). Interestingly, the presence of fines (i.e., smaller polymer spheres,

Figures S11 and S12) in the pre-polymerized catalyst is suggestive of high or even uncontrolled catalyst activity at reaction onset (Figure 4c). The high monomer concentration at 7.5 bar, together with a relatively high concentration of co-catalyst (6.5 eq. TiBA), is likely to have contributed to substantial polymerization rates at the particles' surfaces. Similar morphologies were, however, also observed at low pressures (i.e., 0.6 bar; Figures S12 and S13). This leads us to believe that the catalyst's high reaction rate is inherently related to the kinetics of its active sites. The presence of smaller silica spheres in the pristine catalyst (Figures S2 and S3) may also contribute the formation of smaller polymer spheres.

In general, the morphology of the pre-polymerized $\text{TiCl}_4/\text{MgCl}_2/\text{SiO}_2$ catalyst is a good example for illustrating correlations between high reaction rates and more extensive contributions from the sectioning mechanism at particle level. By adopting milder reaction conditions, diffusion limitations, imposed on both the monomer and the co-catalyst, may be reduced. This can facilitate a more controlled fragmentation of the catalyst via a layer-by-layer mechanism at particle and support domain (granulate) level. In fact, for a $\text{TiCl}_4/\text{MgCl}_2/\text{SiO}_2$ catalyst sample pre-polymerized in gas-phase at ambient pressure and at lower co-catalyst concentration (3.25 eq. TiBA, room temperature, Figure 6), layer-by-layer fragmentation was predominantly observed in the particle interiors. In addition to this, no thick surface layer of polymer was formed. This proves that the reaction conditions significantly affect mass transport and thus the degree to which a particular fragmentation pathway contributes. The formation of large void spaces, as observed for particles $\text{ZN}_{7.5-2}$ and $\text{ZN}_{7.5-4}$, may be linked to the dominance of the sectioning mechanism and may be contained by polymerizing under milder conditions, hence ensuring a higher bulk density of the product.

The morphological insights acquired on the high activity $\text{TiCl}_4/\text{MgCl}_2/\text{SiO}_2$ catalyst are also consistent with recent investigations by our group that revealed correlations between faster catalyst kinetics and a higher relative contribution of the sectioning

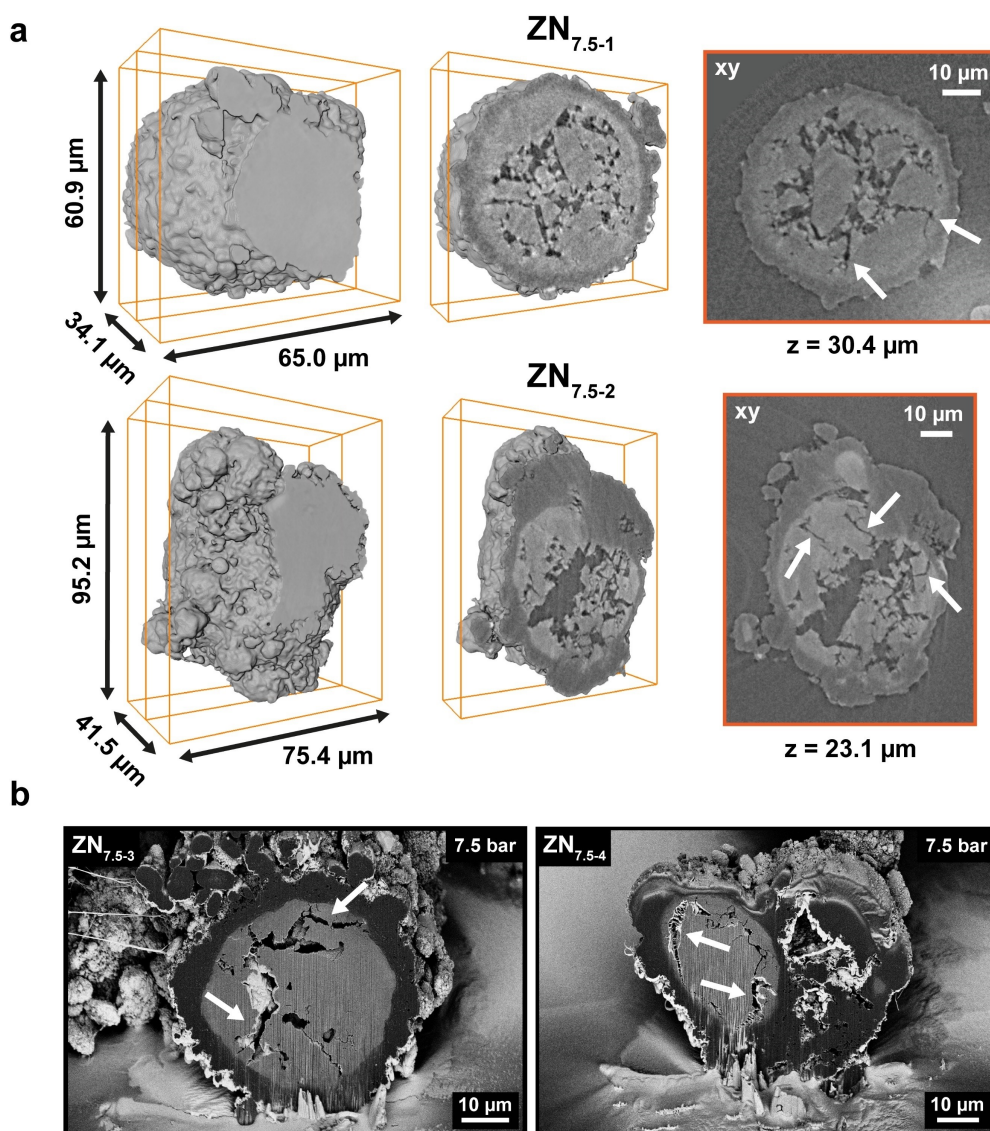


Figure 5. Morphological characterization of the $\text{TiCl}_4/\text{MgCl}_2/\text{SiO}_2$ catalyst pre-polymerized at 7.5 bar ethylene pressure (1 min, room temperature, slurry-phase, 6.5 eq. triisobutylaluminum (TIBA), obtained yield: 6.4 $\text{g}_{\text{PE}}/\text{g}_{\text{cat}}$): (a) Reconstructed tomographies and corresponding virtual cross-sections of two particles designated as $\text{ZN}_{7.5-1}$ and $\text{ZN}_{7.5-2}$. The light gray phase can be classified as support-dominant phase, while the dark gray phases correspond to the remaining particle volume (i. e., polymer-dominant phase + pore space). z is the depth of a given cross-section (xy) with $z = 0 \mu\text{m}$ corresponding to the top of the particle. The formation of large cracks (i. e., sectioning) is indicated by white arrows. (b) Scanning electron microscopy (SEM; light gray, silica support; dark gray, polymer) images of the cross-sections of two particles from the same batch ($\text{ZN}_{7.5-3}$ and $\text{ZN}_{7.5-4}$).

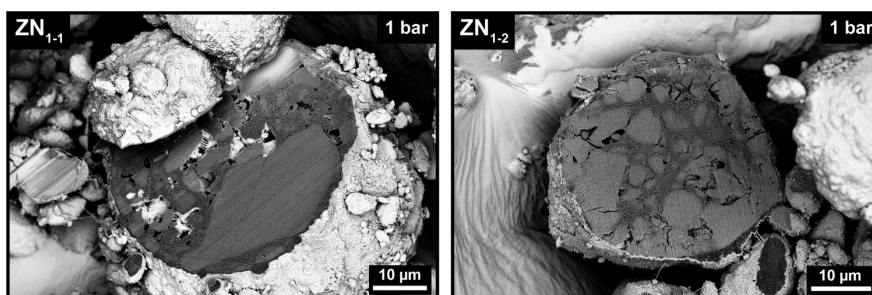


Figure 6. Scanning electron microscopy (SEM; light gray, silica support; dark gray, polymer) images of two $\text{TiCl}_4/\text{MgCl}_2/\text{SiO}_2$ catalyst particles (ZN_{1-1} and ZN_{1-2}) that were pre-polymerized in gas-phase for 60 min at 1 bar ethylene pressure (1 mL/min, room temperature, 3.25 eq. triisobutylaluminum, yield not determined).

mechanism during gas-phase ethylene polymerization in metal-locene-based catalysts.^[12]

Conclusions

New insights into the factors regulating the fragmentation behaviour of industrial-grade, silica-supported olefin polymerization catalysts were gained using a combination of X-ray microscopy (i.e., laboratory-based nanoCT) and electron microscopy (FIB-SEM). A low macroporosity of the support, a high accessibility of a particle's interior volume during the early reaction stages, as well as fast polymerization kinetics were found to favour the occurrence of the sectioning mechanism, both at the silica domain and catalyst particle level. In general, the contributions of the sectioning pathway to the fragmentation of a given catalyst particle are governed by the degree of mass transfer limitations and stress imposed upon a catalyst particle, which, in turn, are related to the catalyst's chemical and physical properties, as well as the applied polymerization conditions. While the cross-sectional analysis via FIB-SEM delivered highly resolved morphological information in 2D, the acquired nanoCT data provided more comprehensive insights into the composition of the catalyst particles, the spatial distribution of residual support domains and fragments, as well as crack formation and distribution in 3D. Our study demonstrates the suitability of laboratory-based nanoCT for research on heterogeneous catalysts, where high resolution morphological and structural data is desired.

Experimental Section

Nano-computed tomography (nanoCT) NanoCT measurements were conducted using a laboratory-based X-ray computed tomography set-up based on lens-free X-ray projection magnification.^[33–35] The set-up features an Excillum Nanotube N2 110 kV (Excillum AB, Kista, Sweden) with a 500 nm thick tungsten transmission target as X-ray source and a DECTRIS EIGER2 R hybrid photon counting detector (DECTRIS AG, Baden-Daettwil, Switzerland) with a CdTe sensor. Additional details on the instrumentation can be found in the publications [32–34]. For each measurement, a pre-polymerized catalyst particle was mounted on the tip of a needle-shaped sample holder using epoxy glue, brought close to the X-ray source and scanned over a range of 360°. Voxel samplings in the range of 93–136.4 nm were used. The nanoCT data was reconstructed using an in-house developed filtered back-projection (FBP) algorithm, after which a phase retrieval was applied.^[33] Both sample drift and irregularities in the sensitivity of the detector pixels were corrected for. An average 3D spatial resolution of 177 nm was obtained based on Fourier Shell Correlation (FSC) analysis in IMAGIC FSC (Image Science Software GmbH, Berlin, Germany) using the half-bit criterion (1/2 bit of information per voxel).^[51] For this, the original 2D projections of each data set were divided by angle into even and odd projections. Each set of projections was reconstructed using the FBP algorithm. The 3D Fourier transforms of both reconstructions were then used to determine their statistical correlation (i.e., normalized cross-correlation coefficient over their corresponding shells) in Fourier space as a function of spatial frequency (1/voxel size). By using the half-bit criterion as FSC threshold, the resolution was estimated as the intersection of the half-bit threshold curve with the FSC (Figure S4). The FSC analysis was performed on the reconstructed data sets prior to further image processing such as

phase retrieval. Only reconstructed particles with well-defined features (e.g., macropores) delivered resolution values in an appropriate range. The resolutions of particles with low degrees of macroporosity were neglected. Additional information on the procedure can be found in previous work by Müller and co-workers.^[33] Post processing and visualization of the reconstructed catalyst particles was performed using the Avizo™ software package by Thermo Fisher Scientific.

Focused ion beam-scanning electron microscopy (FIB-SEM) FIB-SEM experiments were performed on individual catalyst particles using a FEI Helios NanoLab G3 UC scanning electron microscope following procedures from literature.^[12,24] The samples were first mounted onto double-sided adhesive, conductive carbon tape, which was attached to an aluminium SEM stub. A Cressington 208HR sputter coater was utilized to apply a Pt coating of ~6 nm thickness. Using a 45° angled SEM stub at different stage tilt angles, the particles were cut parallel to the surface of the stub. The cross-sectional images were acquired in backscattered electron (BSE) mode at 2 kV and 0.1 nA using a Through the Lens Detector (TLD) and an immersion lens.

Diffuse reflectance infrared Fourier transform spectroscopy (DRIFTS) DRIFTS experiments were performed *in situ* using a Bruker Tensor 37 spectrometer, equipped with a nitrogen cooled MCT (mercury cadmium telluride) detector, and a Harrick Praying Mantis™ High Temperature Reaction Chamber. For each measurement, the sample cup of the reaction chamber was loaded inside a nitrogen glovebox with a small amount of glass wool, a VICI Jour® stainless steel frit and 12 mg of the catalyst. While the Zr/MAO/SiO₂ catalyst did not require any form of activation, the TiCl₄/MgCl₂/SiO₂ catalyst was treated with 1.5 eq. triisobutylaluminum (TiBA) in pentane and subsequently dried. For each experimental run, the loaded reaction cell was transferred to the spectrometer and connected to the gas lines. All experiments were performed in gas-phase at room temperature using an ethylene flow of 5 mL/min at 1 bar. To avoid contamination and deactivation of the sample, the gas lines were flushed with nitrogen for 10 min before introducing ethylene to the reaction cell. FT-IR spectra were recorded in 30 s intervals in the spectral range of 900–4500 cm⁻¹ with a 4 cm⁻¹ resolution and 16 s scan time. The data were evaluated using an in-house developed MATLAB™ code. First, the spectra were normalized to the highest band at approximately 1279 cm⁻¹. A background subtraction was then performed on all spectra using a normalized spectrum of the catalyst that was recorded under nitrogen atmosphere before the reaction. After reducing the spectral range to 2800–3200 cm⁻¹, Principal Component Analysis (PCA) was applied to the first five spectra that were recorded in the presence of ethylene. The first Eigenspectrum (first principal component) of each data set was fitted via a Least Squares Linear Combination (LSLC) fitting with 8 manually assigned pseudo-Voigt peaks (2851, 2890, 2920, 2958, 2988, 3011, 3077 and 3124 cm⁻¹; 2800 cm⁻¹ and 3200 cm⁻¹ defined as boundaries for fitting). The area of the peak fitted to the symmetric CH₂ stretching vibration band at 2851 cm⁻¹ was evaluated as a function of time. A polymerization rate was obtained from the first time derivative of this time evolution. All reported activity plots are based on the most active runs of the respective catalysts and were verified with a second measurement.

Acknowledgments

The research was funded by a grant from the Dutch Polymer Institute (DPI, P.O. Box 902, 5600 AX Eindhoven, The Netherlands) and represents a part of the Research Program of DPI project no. 813. F.M. acknowledges additional funding from a Netherlands Organization for Scientific Research (NWO) VIDI grant (723.015.007). We would like to thank Dr. Jochem Wijten (Utrecht University) for

recording some of the SEM data on the pre-polymerized Zr/MAO/ SiO_2 catalyst.

Conflict of Interest

The authors declare no conflict of interest.

Data Availability Statement

The data that support the findings of this study are available from the corresponding author upon reasonable request.

Keywords: Computed Tomography · Catalyst Fragmentation · Metallocenes · Olefin Polymerization · Ziegler-Natta

- [1] D. W. Sauter, M. Taoufik, C. Boisson, *Polymer* **2017**, *9*, 1–13.
- [2] J. B. P. Soares, T. F. L. McKenna, *Polyolefin Reaction Engineering*, Wiley-VCH, Weinheim, Germany **2012**.
- [3] J. R. Severn, J. C. Chadwick, R. Duchateau, N. Friederichs, *Chem. Rev.* **2005**, *105*, 4073–4147.
- [4] A. Alizadeh, T. F. L. McKenna, *Macromol. React. Eng.* **2018**, *12*, 1700027.
- [5] G. Weickert, G. B. Meier, J. T. M. Pater, K. R. Westerterp, *Chem. Eng. Sci.* **1999**, *54*, 3291–3296.
- [6] X. Zheng, M. Smit, J. C. Chadwick, J. Loos, *Macromolecules* **2005**, *38*, 4673–4678.
- [7] B. Horáčková, Z. Grof, J. Kosek, *Chem. Eng. Sci.* **2007**, *62*, 5264–5270.
- [8] F. Machado, E. L. Lima, J. C. Pinto, T. F. McKenna, *Polym. Eng. Sci.* **2010**, *51*, 302–310.
- [9] K. W. Bossers, R. Valadian, S. Zaroni, R. Smeets, N. Friederichs, J. Garrovoet, F. Meirer, B. M. Weckhuysen, *J. Am. Chem. Soc.* **2020**, *142*, 3691–3695.
- [10] K. W. Bossers, R. Valadian, J. Garrovoet, S. van Malderen, R. Chan, N. Friederichs, J. Severn, A. Wilbers, S. Zaroni, M. K. Jongkind, B. M. Weckhuysen, F. Meirer, *JACS Au* **2021**, *1*, 852–864.
- [11] S. Zaroni, N. Nikolopoulos, A. Welle, A. Vantomme, B. M. Weckhuysen, *Catal. Sci. Technol.* **2021**, *11*, 5335–5348.
- [12] M. J. Werny, J. Zarupski, I. C. ten Have, A. Piovano, C. Hendriksen, N. H. Friederichs, F. Meirer, E. Groppo, B. M. Weckhuysen, *JACS Au* **2021**, *1*, 1996–2008.
- [13] M. J. Werny, R. Valadian, L. M. Lohse, A.-L. Robisch, S. Zaroni, C. Hendriksen, B. M. Weckhuysen, F. Meirer, *Chem Catalysis* **2021**, *1*, 1413–1426.
- [14] V. W. Buls, T. L. Higgins, *J. Polym. Sci. Part A* **1970**, *8*, 1037–1053.
- [15] M. Kakugo, H. Sadatoshi, M. Yokoyama, K. Kojima, *Macromolecules* **1989**, *22*, 547–551.
- [16] M. A. Ferrero, R. Sommer, P. Spanne, K. W. Jones, W. C. Conner, *J. Polym. Sci. Part A* **1993**, *31*, 2507–2512.
- [17] J. T. M. Pater, G. Weickert, J. Loos, W. P. M. Van Swaaij, *Chem. Eng. Sci.* **2001**, *56*, 4107–4120.
- [18] X. Zheng, J. Loos, *Macromol. Symp.* **2006**, *236*, 249–258.
- [19] G. Fink, B. Steinmetz, J. Zechlin, C. Przybyla, B. Tesche, *Chem. Rev.* **2000**, *100*, 1377–1390.
- [20] Y. J. Jang, C. Naundorf, M. Klapper, K. Müllen, *Macromol. Chem. Phys.* **2005**, *206*, 2027–2037.
- [21] C. Wu, P. T. Williams, *Appl. Catal. B* **2010**, *96*, 198–207.
- [22] C. Ziegler, S. Thiele, R. Zengerle, *J. Power Sources* **2011**, *196*, 2094–2097.
- [23] R. Singh, A. R. Akhgar, P. C. Sui, K. J. Lange, N. Djilali, *J. Electrochem. Soc.* **2014**, *161*, F415–F424.
- [24] D. A. M. De Winter, F. Meirer, B. M. Weckhuysen, *ACS Catal.* **2016**, *6*, 3158–3167.
- [25] Y. Fam, T. L. Sheppard, A. Diaz, T. Scherer, M. Holler, W. Wang, D. Wang, P. Brenner, A. Wittstock, J. D. Grunwaldt, *ChemCatChem* **2018**, *10*, 2858–2867.
- [26] R. Mayorga-González, M. Rivera-Torrente, N. Nikolopoulos, K. W. Bossers, R. Valadian, J. Yus, B. Seoane, B. M. Weckhuysen, F. Meirer, *Chem. Sci.* **2021**, *12*, 8458–8467.
- [27] J. Wirth, S. Englisch, D. Drobek, B. Apeleo Zubiri, M. Wu, N. Taccardi, N. Raman, P. Wasserscheid, E. Spiecker, *Catalysts* **2021**, *11*, 810.
- [28] B. Apeleo Zubiri, J. Wirth, D. Drobek, S. Englisch, T. Przybilla, T. Weissenberger, W. Schwieger, E. Spiecker, *Adv. Mater. Interfaces* **2021**, *8*, 2001154.
- [29] Q. Meyer, J. Hack, N. Mansor, F. Iacoviello, J. J. Bailey, P. R. Shearing, D. J. L. Brett, *Fuel Cells* **2019**, *19*, 35–42.
- [30] T. M. M. Heenan, C. Tan, J. Hack, D. J. L. Brett, P. R. Shearing, *Mater. Today* **2019**, *31*, 69–85.
- [31] T. M. M. Heenan, D. P. Finegan, B. Tjaden, X. Lu, F. Iacoviello, J. Millichamp, D. J. L. Brett, P. R. Shearing, *Nano Energy* **2018**, *47*, 556–565.
- [32] F. Lutter, P. Stahlhut, K. Dremel, S. Zabler, J. Fell, H. G. Herrmann, R. Hanke, *Nucl. Instrum. Methods Phys. Res. Sect. B* **2021**, *500–501*, 10–17.
- [33] D. Müller, J. Graetz, A. Balles, S. Stier, R. Hanke, C. Fella, *Crystals* **2021**, *11*, 677.
- [34] C. Fella, J. Dittmann, D. Müller, T. Donath, D. Murer, T. Tuohimaa, A. Sofienko, S. Zabler, R. Hanke, *Microsc. Microanal.* **2018**, *24*, 234–235.
- [35] J. Graetz, D. Müller, A. Balles, C. Fella, *J. Instrum.* **2021**, *16*, P01034–P01034.
- [36] L. Seda, A. Zubov, M. Bobak, J. Kosek, A. Kantzas, *Macromol. React. Eng.* **2008**, *2*, 495–512.
- [37] L. Meisterová, A. Zubov, K. Smolná, F. Štěpánek, J. Kosek, *Macromol. React. Eng.* **2013**, *7*, 277–288.
- [38] G. Fink, B. Tesche, F. Korber, S. Knoke, *Macromol. Symp.* **2001**, *173*, 77–87.
- [39] S. Knoke, D. Ferrari, B. Tesche, G. Fink, *Angew. Chem. Int. Ed.* **2003**, *42*, 5090–5093; *Angew. Chem.* **2003**, *115*, 5244–5248.
- [40] J. M. Zhou, N. H. Li, N. Y. Bu, D. T. Lynch, S. E. Wanke, *J. Appl. Polym. Sci.* **2003**, *90*, 1319–1330.
- [41] X. Zheng, M. Smit, J. C. Chadwick, J. Loos, *Macromolecules* **2005**, *38*, 4673–4678.
- [42] H. Hammawa, S. E. Wanke, *Polym. Int.* **2006**, *55*, 426–434.
- [43] G. A. H. Nooijen, *Catal. Today* **1991**, *11*, 35–46.
- [44] F. M. Silva, J. P. Broyer, C. Novat, E. L. Lima, J. C. Pinto, T. F. McKenna, *Macromol. Rapid Commun.* **2005**, *26*, 1846–1853.
- [45] A. Di Martino, G. Weickert, T. F. L. McKenna, *Macromol. React. Eng.* **2007**, *1*, 165–184.
- [46] T. F. L. McKenna, E. Tioni, M. M. Ranieri, A. Alizadeh, C. Boisson, V. Monteil, *Can. J. Chem. Eng.* **2013**, *91*, 669–686.
- [47] E. L. Weist, A. H. Ali, B. G. Naik, W. C. Conner, *Macromolecules* **2002**, *22*, 3244–3250.
- [48] A. Piovano, K. S. Thushara, E. Morra, M. Chiesa, E. Groppo, *Angew. Chem. Int. Ed.* **2016**, *55*, 11203–11206; *Angew. Chem.* **2016**, *128*, 11369–11372.
- [49] A. Piovano, P. Pletcher, M. E. Z. Velthoen, S. Zaroni, S. H. Chung, K. Bossers, M. K. Jongkind, G. Fiore, E. Groppo, B. M. Weckhuysen, *ChemPhysChem* **2018**, *19*, 2662–2671.
- [50] G. A. H. Nooijen, *Eur. Polym. J.* **1994**, *30*, 11–15.
- [51] M. Van Heel, M. Schatz, *J. Struct. Biol.* **2005**, *151*, 250–262.

Manuscript received: January 17, 2022
 Revised manuscript received: August 3, 2022
 Accepted manuscript online: August 4, 2022
 Version of record online: October 6, 2022